Global Arable Land Is Shifting Toward the Tropics and Drylands Under Urbanization

Lun Gao[a, b, *], Xiaoman Lu[b], Weston Anderson[c, d, e], Corey Lesk[f, g, h], Elise Mazur[i], Fred Stolle[i], Peter Potapov[i], Francesco N. Tubiello[j], Steffen Fritz[k], Jiafu Mao[b], Liangzhi You[l, m], Deepak Ray[a]

[a] Institute on the Environment, University of Minnesota, St. Paul, MN, USA

[b] Environmental Sciences Division, Oak Ridge National Laboratory, Oak Ridge, TN, USA

[c] Earth System Science Interdisciplinary Center, University of Maryland, College Park, MD, USA

[d] NASA Goddard Space Flight Center, Earth Science Division, Greenbelt, MD, USA

[e] Geographical Sciences, University of Maryland, College Park, MD, USA

[f] Department of Earth and Atmospheric Science, University of Quebec in Montreal, Montreal, QC, Canada

[g] Department of Geography, Dartmouth College, Hanover, NH, USA

[h] Neukom Institute for Computational Science, Dartmouth College, Hanover, NH, USA

[i] World Resources Institute, Washington, DC, USA

[j] Statistics Division, Food and Agriculture Organization of the United Nations, Rome 00153, Italy

[k] International Institute for Applied Systems Analysis (IIASA), Schlossplatz 1, A-2361 Laxenburg, Austria

[l] International Food Policy Research Institute, Washington, DC, USA

[m] Digital Agricultural Research Institute, College of Economics and Management, Huazhong Agricultural University, Wuhan, Hubei, China

Supplementary Methods

Global arable land mapping data. We constructed 1-km Global Arable Land Fraction (GALF) by integrating multiple global satellite-derived land cover products with long-term temporal coverage (≥20 years) and high spatial resolution (≤500 m), selecting only those with consistent temporal characteristics and spatial continuity. The FROM-GLC product[46] was excluded due to variability in input scene timing that affected spatial coherence, while certain regional land cover products were also omitted to maintain consistency across regions. The included global products are the International Geosphere-Biosphere Programme (IGBP) from the Moderate Resolution Imaging Spectroradiometer (MODIS, MCD12Q1 v061)[47], European Space Agency's Climate Change Initiative (CCI)[48], GlobeLand30[49], Global Land Analysis and Discovery (GLAD) dataset[50], and GLC_FCS30D[51]. Detailed specifications on cropland definitions, spatial resolutions, and temporal coverages for each dataset are provided in **Table S1**. Note that for datasets that do not explicitly distinguish arable land from woody croplands, we hereinafter refer to all such areas collectively as cropland.

As shown in **Table S1** and discussed previously[5], cropland definitions vary across products and deviate from the FAO cropland definition, which includes both arable land and permanent woody crops. This introduces possible bias in our and similar analyses. For instance, three products (CCI, GlobeLand30, and GLC_FCS30D) include permanent crops, mostly woody tree crops (e.g., oil palm, cocoa, coffee, rubber, fruit orchards). Conversely, MODIS and GLAD cropland maps exclude them. Furthermore, it is likely that the annual crops component of all products is in fact aligned more with the FAO definition of temporary crops rather than arable land[5]. This is because satellite-derived products, by their nature, primarily reflect land cover, whereas cropland represents a combination of land cover and land use shaped by human activities for food production[52], which are more difficult to distinguish from space. Relying solely on individual land cover datasets could therefore lead to systematic over- or underestimation of cropland extent, particularly in regions dominated by woody crops, such as Southeast Asia.

New method to harmonize across global arable land datasets. To harmonize different products and enhance consistency with the FAO definition of arable land, we developed a synergy approach[53-58] for generating GALF, the workflow of which is illustrated in **Fig. S1**. Unlike previous studies[53-58], we focused exclusively on arable land rather than including permanent crops for the following reasons: (1) arable land is consistently represented across land cover products and FAO statistics (**Table S1**), and (2) the harmonization and validation of GALF rely on ground reference samples[46,59-62] that are typically interpreted from satellite or aerial imagery, which could mix woody crops with forests due to their tree-like canopy structure and phenological characteristics. In other words, even if synergized cropland maps were generated following the FAO cropland definition (i.e., including both arable land and permanent crops), it would be difficult to reliably validate the permanent crop component.

In constructing GALF, the synergy approach integrates five land cover products with FAO country-level arable land statistics (FAOSTAT)[63], considering only the arable land components for products that explicitly distinguish them from woody crops. Woody vegetation was further excluded using the GLAD tree cover mask[50]. The approach assumes that strong agreement among input layers increases confidence in arable land presence (**Fig. S2**), which generally leads to improved mapping accuracy[54-58]. Given that most agreement scores can result from multiple combinations of land cover products (**Fig. S3**), this method first requires ranking the performance of each individual product. Unlike previous studies that rely solely on expert judgment, ground reference samples, or FAOSTAT for ranking[54-58], our approach ranks the products based on both their accuracy against ground reference samples and their consistency with FAOSTAT. This is based on the assumption that the product with the highest accuracy against ground reference samples should also show the closest agreement with FAOSTAT country-level arable land area, provided that sufficient validation samples are available and the FAO statistics are reliable. Specifically, for each country, land cover products were first evaluated and ranked by their overall accuracy when at least 20 validation samples were available, considering some countries with small land areas. To avoid overinterpreting marginal differences, only two decimal places of overall accuracy were considered[56]. In cases where products had identical accuracy or fewer than 20 validation samples were available, the product whose arable land area was closest to the FAOSTAT was assigned a higher rank. In some regions lacking FAOSTAT, rankings were based on continental-scale validation results across nine continental regions (**Fig. S4**), which were delineated according to administrative boundaries[64] and the spatial clustering patterns of global arable land (**Fig. 1a**). More information on ground samples and the performance evaluation of land cover products are provided in the section below.

Once country-level performance rankings of input land cover products were available, an agreement-ranking score lookup table was established based on binary permutations to prioritize high-ranked regions that best matched reference data (**Table S2**). Different from previous research that converted binary permutations to either agreement scores[54-57] or binary scores[58], this study combined both scoring approaches to enhance the likelihood of identifying the optimal configuration that best aligns with ground validation samples and FAO statistics. This is because we found that each scoring method has inherent limitations, but they offer complementary strengths when used together. The agreement-score approach[54-57] prioritizes regions where multiple products consistently indicate the presence of arable land (**Fig. S3**). This method is particularly effective in regions where the input land cover products have comparable accuracy; however, it may underperform in cases where one product significantly outperforms the others. For example, if a single product accurately captures the full extent of arable land, it may mistakenly prioritize regions where multiple lower-performing products indicate arable land over areas correctly identified by the high-performing product alone. Conversely, the binary-score approach[58] gives priority to regions identified by the best-performing product but may be less effective when multiple products exhibit similar accuracy (**Fig. S3**). Thus, combining both approaches increases the diversity of scoring combinations and enhances the ability to identify the configuration that best matches ground validation samples and FAO statistics. In this study, applying the combined method to five input products resulted in a total of 58 unique scoring combinations, whereas using either approach alone yielded only 32 combinations (i.e., 2^5; see **Table S2**).

Then, the ground samples and FAOSTAT were used again as benchmarks to identify the best-performing scoring combinations. We found that the combination yielding the highest overall accuracy did not always align with the one most closely matching the FAOSTAT-reported arable land area, particularly in African countries. This discrepancy is likely attributable to relatively low agreement among five land cover products over Africa (**Fig. S2**) and the inherent uncertainties in both the ground reference and FAOSTAT data[65]. To balance both criteria, for countries with more than 20 validation samples, we retained only those combinations that either exceeded the overall accuracy of the best individual product or ranked within the top 10% of all combinations based on overall accuracy. Among these, the combination with the closest arable land area to the FAOSTAT was selected. For countries lacking sufficient validation samples, the FAOSTAT alone was used to select the best combination. In cases where FAOSTAT data were unavailable, but more than 20 validation samples were present, ground samples were directly used to identify the optimal combination. For regions lacking both adequate validation samples and FAOSTAT data, the best combination was selected based on the corresponding continental validation results.

Finally, the 1-km GALF was computed by averaging arable land weights at 100-m subpixels within areas defined by the optimal scoring combination. Considering that the spatial resolution varies across input land cover datasets, all products were first reprojected into a common coordinate system (WGS84; EPSG:4326) and resampled to a 100-m resolution to facilitate the calculation of arable land fractions at the 1-km scale. In this calculation, 100-m pixels classified as pure arable land by all overlapping products were assigned a weight of 1, while pixels identified as mosaics (i.e., a mix of cropland and other land cover types) by any product were assigned lower weights to reflect their partial arable land composition. Specifically, for CCI, mosaic cropland classes were weighed as 0.75 when cropland fraction exceeded 50%, and 0.25 when it was below 50%. For MODIS, mosaic cropland comprising 40–60% cultivated land was assigned a value of 0.5. In cases where a 100-m pixel was simultaneously labeled as pure arable land and mosaic arable land by different products, the assigned weight was averaged accordingly. Notably, a few small islands were not represented in the continental mask[64], for which the arable land fraction was directly calculated based on the GLAD dataset[50] due to its similarity to the FAO arable land definition, high spatial resolution, and reliable accuracy, as discussed below. We implemented the procedure using data from 2010 to identify the optimal scoring combination, which was then applied to generate GALF for the years 2000, 2010, and

2020. These three years represent the intersection of temporal coverage across all products, with MODIS land cover from 2001 used as a proxy for 2000.

It should be noted that, although the proposed method is expected to produce high-quality arable land maps beyond the capabilities of individual land cover products, its performance strongly depends on the quality of the input datasets and may fail to capture arable land in regions where most products perform poorly. One notable example is greenhouse agriculture, which should ideally be detected by all land cover products but exhibits distinct spectral reflectance compared with other arable land[66]. We found that the ability of the products to detect greenhouse infrastructures varies considerably. As examined, while small- to medium-sized greenhouse facilities, such as those in Michoacán, Mexico (19.9°N, 102.2°W), are generally captured by all products, only GlobeLand30 and CCI successfully detect the large-scale greenhouse infrastructures (> 500 km^2) in Almería, Spain (36.7°N, 2.7°W)[67,68]. In contrast, other products misclassify these areas as impervious surfaces (GLC_FCS30D), wetlands (GLAD), or non-vegetated land (MODIS). Consequently, the proposed method cannot reliably capture these large-scale greenhouse areas in Spain. To address this issue, we explicitly identified these greenhouse areas across Spain by combining GlobeLand30 and CCI arable land layers with GLC_FCS30D impervious surfaces and GLAD wetlands across Spain, before calculating the 1-km arable land fraction. **Fig. S5** demonstrates that this combined approach effectively captures the greenhouse areas in southern Spain. On the other hand, in Africa and the Arabian Peninsula, the quality and agreement among the five input cropland products were sometimes very low (**Fig. S2**). For example, GLC_FCS30D missed an entire scene in Sudan, while CCI misclassified several roads within the Congolian rainforests as cropland. Therefore, we carefully compared GALF with GLAD by evaluating their overall accuracy, area consistency with FAOSTAT statistics, and spatial patterns of arable land distribution. Based on the assessment, we replaced GALF with GLAD in the Republic of the Congo, Democratic Republic of the Congo, South Sudan, Sudan, Somalia, and Saudi Arabia, where GLAD demonstrated comparable accuracy to GALF but provided more realistic spatial patterns.

To the best of our knowledge, GALF is the first global long-term arable land fraction product, providing a novel framework for assessing arable land dynamics in the 21st century.

Performance evaluation of input land cover products. To support the performance ranking of land cover products in 2010 and identify the best scoring combination, we compiled multiple sources of reference samples (**Fig. S6**). The year 2010 was selected because it represents the midpoint of the study period and offers the most consistent availability of ground validation data. The reference samples included two datasets from Tsinghua University[46,59] and additional samples from the Geo-wiki crowdsourcing platform[60] and the U.S. Geological Survey's Land Change Monitoring, Assessment and Projection (LCMAP)[61]. The Tsinghua University datasets[46,59] were originally developed to support the creation and validation of their 30-m global land cover product (i.e., FROM-GLC), where cropland is defined as arable and tillage land with herbaceous and/or shrub crops—thus more than arable land. The first dataset[46] involves 36,352 globally distributed random samples, manually labeled by hundreds of students, researchers, and experts using Google Earth imagery in or around 2010. The second dataset[59] contains 38,664 global random sample units spanning the years 1986 to 2010, derived through interpretation of Landsat imagery[69], MODIS enhanced vegetation index (EVI)[70], and other high-resolution images via Google Earth. For this study, a total of 11,672 samples in 2010 were considered. The Geo-wiki dataset[60,71] records the dominant, secondary, and tertiary land cover types, with cropland defined as "cultivated and managed" or "mosaic of cultivated and managed/natural vegetation". In this study, locations falling into any of the three cropland-related categories were considered as reference. It comprises 151,942 globally distributed random samples derived from the visual interpretation of Google Earth imagery before 2012. A subset of 12,555 samples from 2010 was selected for analysis. The LCMAP reference dataset[61] defines cropland as areas used for the production of crops, including cultivated and uncultivated croplands, hay fields, orchards, vineyards, and pasturelands actively managed for crop production. It offers annual land cover labels for approximately 25000 random locations across the contiguous United States (CONUS) from 1984 to 2021 based on systematic interpretation of Landsat imagery and aerial photographs. A subset of 24,995 samples from 2010 was used in this study. To integrate the four sample sets and avoid conflicting validation results, samples located within the same 1-km pixel were merged, and those indicating different land cover types were excluded. A 1-km resolution was adopted to ensure consistency in comparisons among the various land cover products and the GALF. This resulted in a final dataset of 61,294 samples.

To validate the performance of different land cover products in mapping arable land, 1-km arable land fraction maps were generated by averaging values from the 100-m resolution layers, where any pixel with an arable land fraction greater than zero was designated as arable land[57]. Following previous studies[54-57], accuracy was quantified using overall accuracy (OA), defined as the probability that a sample is correctly classified—i.e., the sum of true positives and true negatives divided by the total number of samples. Continental and global validation results for the five land cover products were summarized in **Table S3**, indicating that MODIS achieved the highest overall accuracy globally and across most continents, followed by GLAD, GlobeLand30, CCI, and GLC_FCS30D. However, despite its strong performance, MODIS cannot be used independently to derive 1-km arable land fractions due to its relatively coarse native resolution of 500 m. These performance rankings, along with country-level validation results and FAOSTAT, form the basis for ranking individual land cover products and identifying the optimal scoring combinations.

Validation of GALF. To independently assess the accuracy of the GALF maps, we conducted a multi-scale validation in 2020 and compared it against other land cover products. Specifically, we first assessed its spatial accuracy using an independent reference sample set[62] (**Fig. S6**), which defines cropland as rainfed and irrigated croplands following the United Nations' Land

Cover Classification rule[72]. This dataset integrates multiple data sources, including high-resolution imagery from Google Earth, vegetation cover, plant phenology, tree height, and terrain characteristics, and comprises 79,112 random samples. To avoid duplicate and conflicting assessment results, samples located within the same 1-km pixel were merged, while those indicating different land cover types were removed, leading to a final dataset of 79,001 samples. Additionally, country-level arable land areas derived from GALF were compared with FAO statistics to evaluate area consistency.

Before presenting the validation results, **Fig. S7** provides an overview of global arable land fraction patterns depicted by the GALF maps for the years 2000, 2010, and 2020. As shown, arable land is predominantly concentrated in the Northern Hemisphere, particularly in North America, Europe, South Asia, and East Asia. By contrast, arable land is more sparsely distributed in low-latitude and Southern Hemisphere regions, including South America, Africa, Southeast Asia, and Oceania. When compared with other land cover products, **Table S4** shows that GALF exhibits strong performance comparable to MODIS on the global scale and across all continents, followed by GLAD, GlobeLand30, CCI, and GLC_FCS30D. At the continental level, GALF outperforms all other products in four out of nine regions, ranking second in four and third in one. Similar results are also observed across different Köppen–Geiger climate zones: GALF achieves the highest accuracy in 12 out of 26 zones, ranks second in 10 zones, and third in four (**Table S5**).

On the other hand, **Fig. S8** compares country-level arable land area estimates from various land cover products against FAO-reported statistics. GALF achieves the highest correlation ($R = 0.993$) and the lowest root mean square error ($RMSE = 2.35 \times 10^4$ km^2), demonstrating superior accuracy in capturing national-scale arable land area. Compared to GLAD and MODIS, GALF improves the correlation by more than 0.6% and reduces RMSE by over 29%. For global total arable land, GLAD (1.32×10^7 km^2), GALF (1.31×10^7 km^2), and MODIS (1.46×10^7 km^2) are closest to the FAO-reported total (1.38×10^7 km^2), while other products (i.e., CCI, GlobeLand30, and GLC_FCS30D) significantly overestimate the global arable land area by more than 0.75×10^7 km^2.

Built-up fraction. The 1-km built-up fraction was calculated using built-up surface data[73,74] from the Global Human Settlement Layer (GHSL) project, developed by the European Commission's Joint Research Centre as part of the Copernicus Emergency Management Service. Built-up surface is defined as the gross building footprint area (including wall thickness) enclosed by the outer building walls. The dataset was generated using a symbolic machine learning–based supervised classification approach[75] applied to Sentinel-2 imagery[76], achieving a high Intersection-over-Union (IoU)[77] score of 0.92, placing it among the most accurate publicly available built-up datasets. The data are temporally interpolated or extrapolated in five-year intervals, covering the period from 1975 to 2030. In this study, 1-km built-up surface data for the years 2000, 2010, and 2020 were extracted and converted into built-up fractions by dividing the built-up area within each grid cell by the cell's total area.

Considering the uncertainties associated with GHSL, we also used the 30-m built-up land data from GLAD[50]. This product defines built-up land as areas containing man-made surfaces—including infrastructure, commercial, and residential land uses—even if such surfaces do not dominate within the pixel. It was produced using a deep learning convolution neural network (CNN) algorithm[78] applied to Landsat imagery, with training data collected from Open Street Map (https://planet.osm.org; https://www.openstreetmap.org). While the overall accuracy was not reported, the user's accuracy ranged from 63.7% to 74.1% and the producer's accuracy from 39.1% to 59.6%. In this study, we computed 1-km built-up fractions by averaging the 30-m GLAD classifications within each 1-km grid cell. Given its relatively low classification accuracy, this dataset was used solely to validate the results presented in the main text (see Supplementary Discussion).

Climate classification. To understand the climatic constraints on arable land and built-up systems, we used the 1-km constant Köppen–Geiger climate classification map[79,80] for the period 1991-2020. The Köppen–Geiger system delineates five major climate zones—tropical (A), arid (B), temperate (C), cold (D), and polar (E)—based on seasonal patterns of monthly temperature and precipitation. Precipitation regimes are further classified as desert (W), steppe (S), fully humid (f), summer dry (s), winter dry (w), and monsoon (m), while temperature regimes include hot (h), cold (k), hot summer (a), warm summer (b), cold summer (c), cold winter (d), tundra (T), and frost (F). This classification scheme has been widely adopted in previously developed Köppen-Geiger climate classification maps[81,82]. Compared with earlier versions that have relatively coarse resolutions (≥0.1°), the product used in this study offers a higher spatial resolution (1 km) and includes corrections for topographic effects. It should be noted that although climate zones shift with rising global temperatures[79,83], they are expected to remain relatively stable over a few decades, as also evidenced by the relatively constant map for the period 1991–2020[79,80].

Historical land cover dynamics. To investigate the historical co-evolution of arable land and built-up areas, we used two long-term land cover reconstructions: the History Database of the Global Environment (HYDE v3.4)[84] and the Land-use Harmonization 2 (LUH2)[85]. HYDE3.4 provides spatially explicit reconstructions of cropland and built-up areas at a resolution of 5 arc minutes. It integrates historical census data, archaeological records, and satellite observations to generate long-term time series from 10,000 BCE to 2024. Its most recent spatial allocation of land use is primarily informed by FAO agricultural land use data and the CCI land cover, supplemented with MODIS imagery and MapBiomas statistics (https://mapbiomas.org/) for Brazil, Indonesia, and China. The historical spatial allocation of built-up areas is estimated by dividing each country's total urban population by its average urban population density, while the allocation of cropland is determined as the residual area after accounting for water bodies, snow and ice, built-up areas, protected lands, and unused regions, which are calibrated using recent land cover products. In this study, we used data from 0 CE onwards. LUH2 offers global annual land-use states from 850 to 2100 at 0.25° resolution, combining historical reconstructions with future projections from integrated assessment models. Designed for Earth system modelling, LUH2 supports CMIP6 by providing consistent trajectories of land-use change, including cropland, pasture, forestry, and urban areas. Its historical land use is based on HYDE v3.2. In this work, we used historical LUH2 data from 850 to 2015. Note that although the definitions of cropland and built-up areas in these datasets differ from those in GALF and GHSL, we expect their historical evolution patterns to be largely consistent at climatic scales.

Supplementary Discussions

Although GALF shows notable improvements over the five other land cover datasets used, and GHSL remains the most accurate publicly available built-up dataset, we further assess the robustness of our findings by replicating all figures using cropland and built-up data from GLAD and historical land-use change from HYDE3.4. Note that GLAD cropland most closely aligns with the FAO definition of arable land among the five land cover products used, although it omits certain categories such as fallow land and temporary meadows and pastures[5].

Replication of Fig. 1 using GLAD data. **Fig. S9** shows that arable land and built-up surface cover about 13.3 and 5.0 million km^2 in 2020. While the total arable land area closely matches that of GALF, the built-up area is over seven times larger than the estimate from GHSL (**Fig. 1**). Consistent with **Fig. 1**, 89% of the cropland and 81% of built-up areas are located in the same ten of the thirty Köppen-Geiger climate classes, including mildly cold (Dfb, Dfa, Dwa), temperate (Cfa, Cwa, Cfb), arid steppe (BSk, BSh), tropical savannah (Aw), and arid desert (BWh). Finer-scale analyses in northwestern Canada, Argentina-Chile, North Africa, northeastern China, and southeastern Australia (**Figs. S9a1-S9c1**) similarly demonstrate strong climate constraints on the cropland and built-up extent. When aggregated across all thirty Köppen–Geiger climate zones, cropland and built-up areas exhibit a strong positive correlation ($R = 0.82$, $p < 0.01$; **Fig. S9d**).

Replication of Fig. 2 using GLAD and LUH2 data. **Fig. S10a** demonstrates the changes in GLAD cropland between 2020 and 2000, with and without concurrent built-up expansion at 0.05° resolution. Largely consistent with **Fig. 2a**, the results show approximately 67% of built-up expansion occurred within 1 km of existing cropland, and that substantial cropland loss across North America, Europe, East Asia, South Asia, and Southeast Asia. Despite notable regional differences from GALF, similar spatial gradients of cropland change were observed across North America (southeast to northwest), the Eurasian Agricultural Belt (west to east), across China (southeast to northwest), and within India (from northern and coastal regions toward central forested areas). In North America, the concurrent decline in cropland alongside built-up area expansion is slightly less pronounced in the southeast, whereas cropland expansion in the northwest is more extensive compared with GALF. In Sub-Saharan Africa, **Fig. S10a** reveals a more pronounced cropland increase without substantial accompanying expansion of built-up areas. In India, **Fig. S10a** shows widespread cropland expansion across central regions, whereas **Fig. 2a** highlights cropland increases primarily concentrated in central forested zones. Despite these differences, both figures consistently demonstrate the strong influence of built-up expansion on cropland dynamics.

Consistent with **Fig. 2b**, **Fig. 10b** shows that 49% of global cropland loss occurred within 1 km of built-up area loss, increasing to 99% within 5 km, where total cropland loss declined sharply with distance from urban contraction. In line with **Fig. 2c**, **Fig. 10c** illustrates that much of the Northern Hemisphere is experiencing land competition between cropland and built-up areas, particularly across North America, Europe, and East Asia. By contrast, low-latitude regions continue to support the concurrent expansion of cropland and urban areas. **Fig. 10d** further confirms that the relationship between cropland and built-up areas can be characterized by three distinct land-use regimes: co-development, stability, and competition.

Replication of Fig. 3 using GLAD data. Consistent with **Fig. 3a**, **Fig. S11a** demonstrates that global cropland increased by 9%—from 12.2 to 13.3 million km^2—between 2000 and 2020, with 11.0 million km^2 remaining stable, 2.3 million km^2 newly cultivated, and 1.2 million km^2 lost. Among them, 89% of net gains occurred in tropical and arid climates, while losses were concentrated in temperate and cold climates, followed by arid and tropical climates (**Fig. S11b**). More specifically, in regions experiencing large-scale cropland displacement, net cropland losses chiefly occurred in the temperate climate while 92% of net gains were concentrated in arid zones. By contrast, in regions undergoing cropland expansion, gains occurred across tropical, arid, and temperate climates, with the tropical zone accounting for the largest share (56%) of the net increase. Overall, these results reaffirm the robustness of the analyses in the main text.

Supplementary Figures

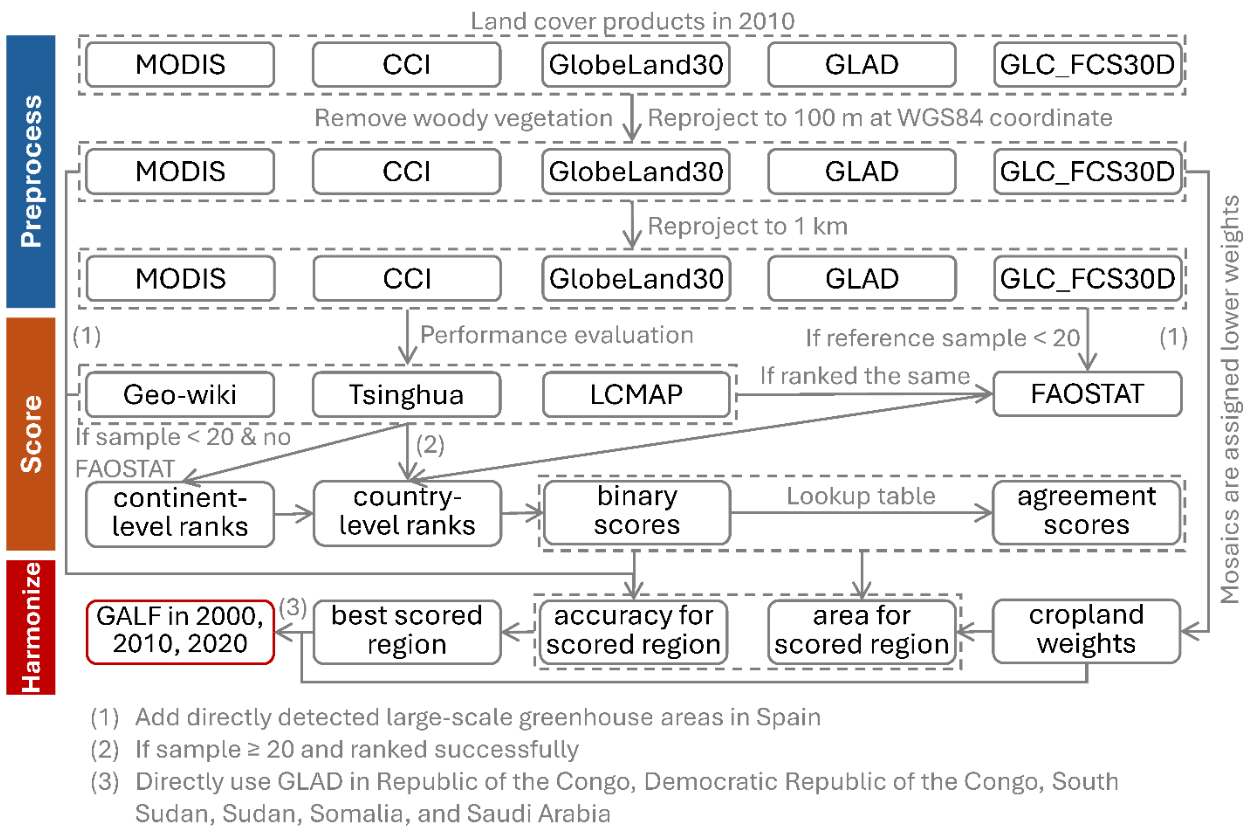

Fig. S1. Flowchart showing the proposed method in calculating the 1-km Global Arable Land Fraction (GALF).

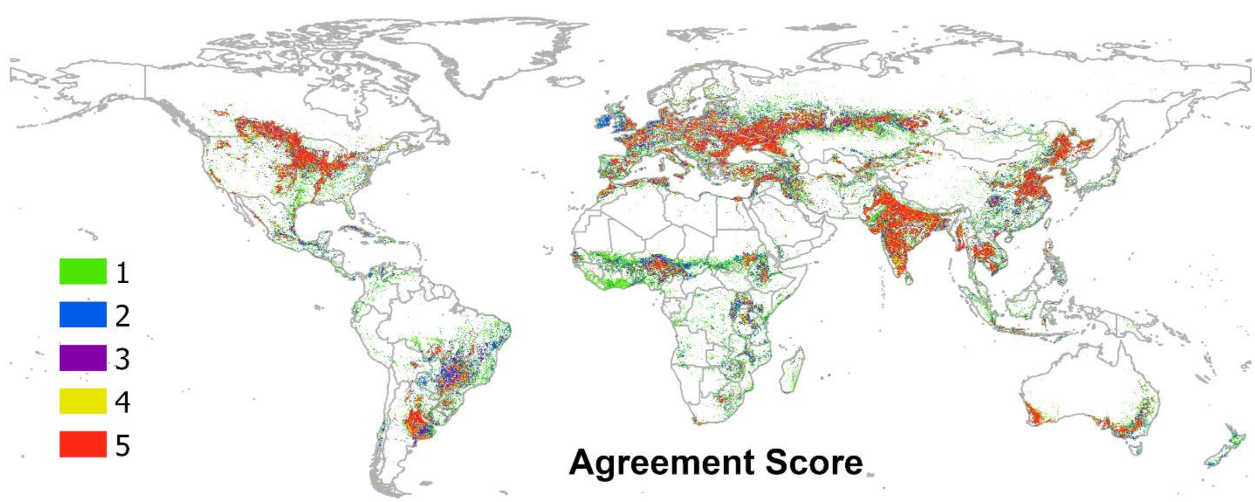

Fig. S2. Agreement scores among five used cropland products (i.e., MODIS, CCI, GlobeLand30, GLAD, and GLC_FCS30D) at 1-km resolution in 2020. A score of 5 indicates that all products consistently identify the presence of cropland.

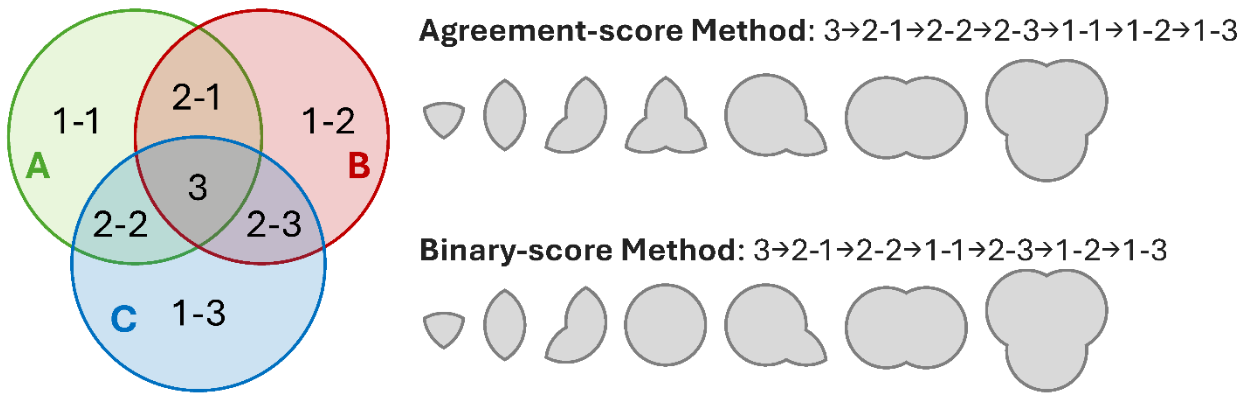

Fig. S3. Schematic diagram illustrating possible permutations among three land cover products, along with the ranking sequences derived from the agreement-score and binary-score methods. Product A represents the highest accuracy product, followed by B and C. In this example, scores "2" and "1" result from three different combinations. The primary difference between the two methods is that the agreement-score method prioritizes region 2-3, whereas the binary-score method prioritizes region 1-1 after accounting for regions 3, 2-1, and 2-2. Notably, the divergence between the two methods increases with the number of input land cover products. Combining both methods expands the set of possible permutations, thereby improving the likelihood of identifying the optimal combination with the highest accuracy against ground validation samples and strongest alignment with FAO arable land statistics.

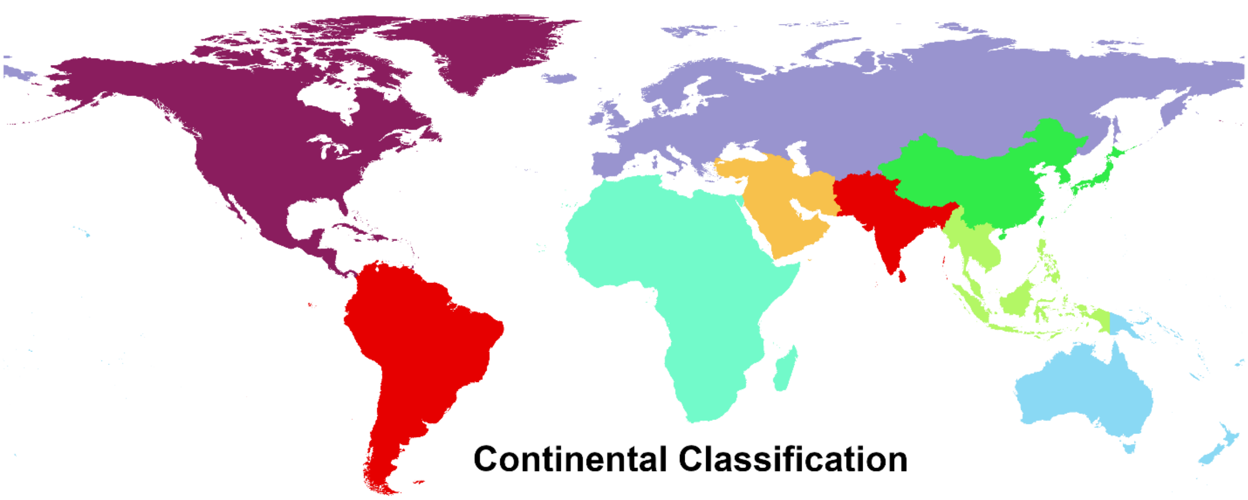

Fig. S4. Classification of nine continental regions based on the Large Scale International Boundary (LSIB)[64]. To reflect the spatial clustering of global arable land (**Fig. 1**), Asia was subdivided into four regions: East Asia, South Asia, Southeast Asia, and Southwest Asia. Meanwhile, Europe, North Asia, and Central Asia were grouped into a single region.

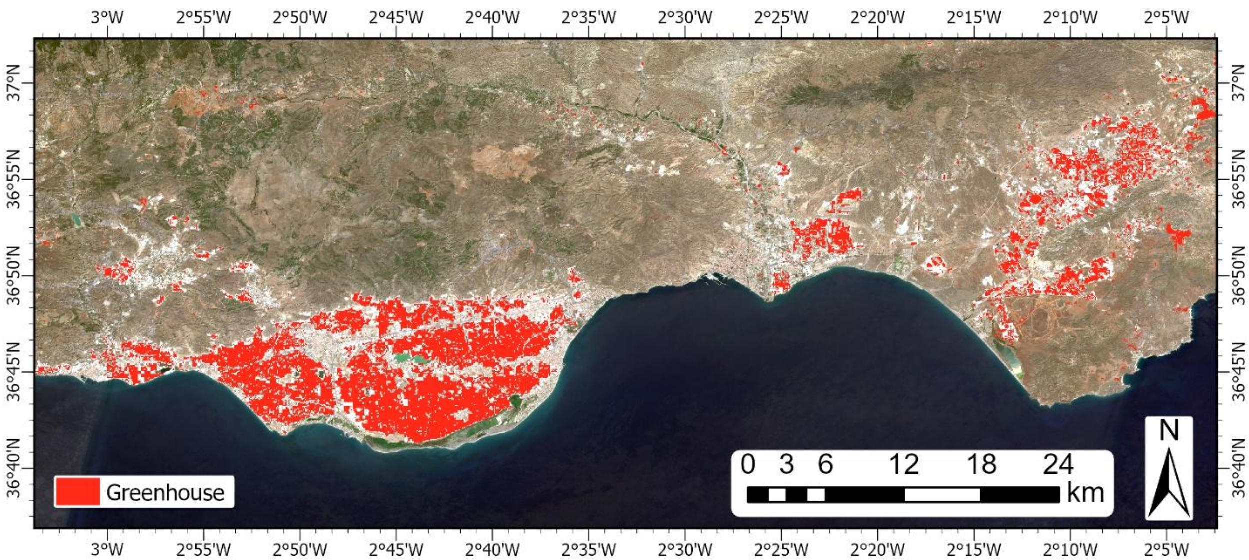

Fig. S5. Detected greenhouses at 1 km in southern Spain in 2020. The mapped greenhouse areas are shown overlaid on Sentinel-2 imagery, where the white regions in the imagery correspond to greenhouse structures.

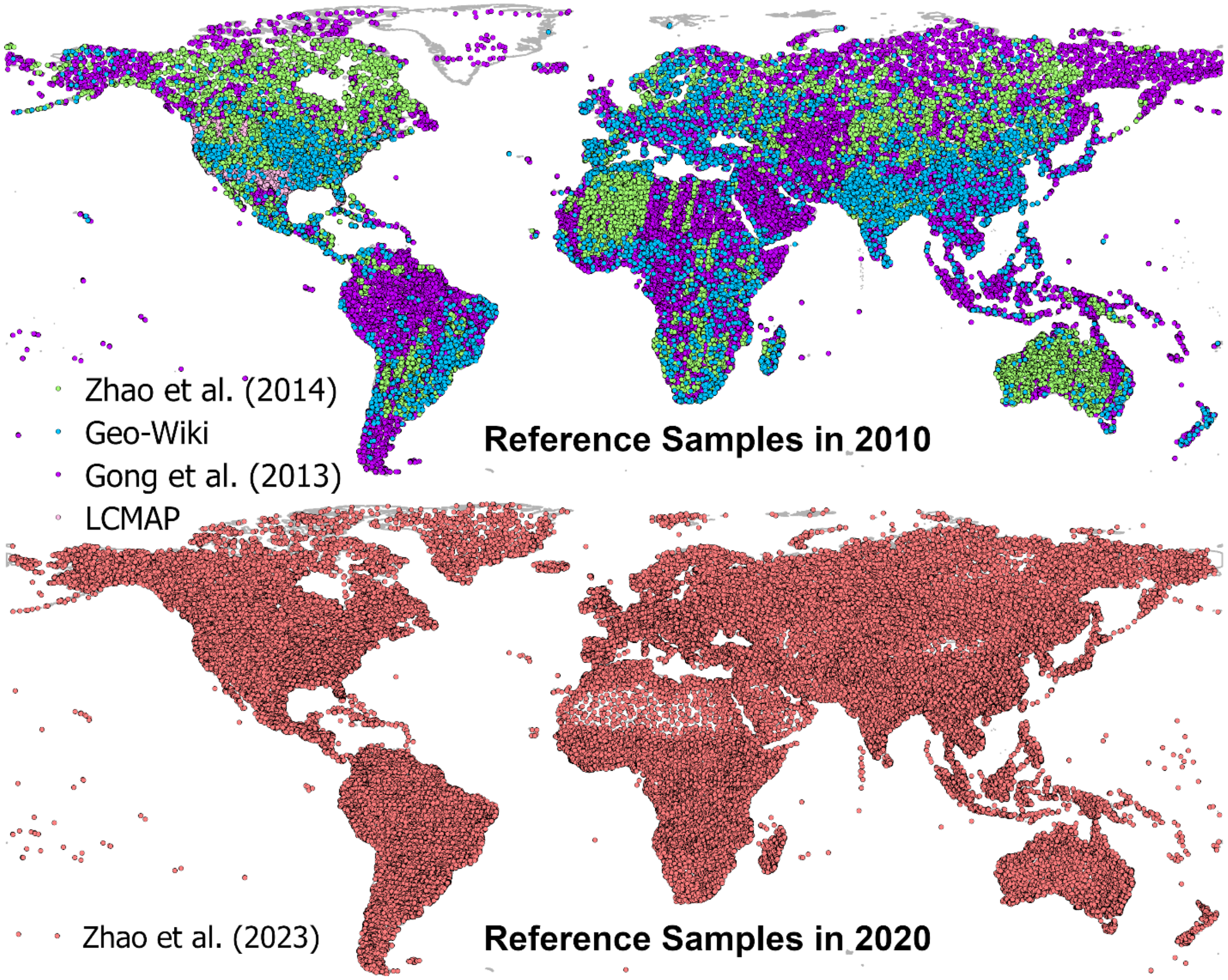

Fig. S6. Geographic distribution of reference samples. Samples in 2010 were used to evaluate satellite-derived land cover products and determine the optimal scoring combination, while samples in 2020 were used to assess the accuracy of the GALF product.

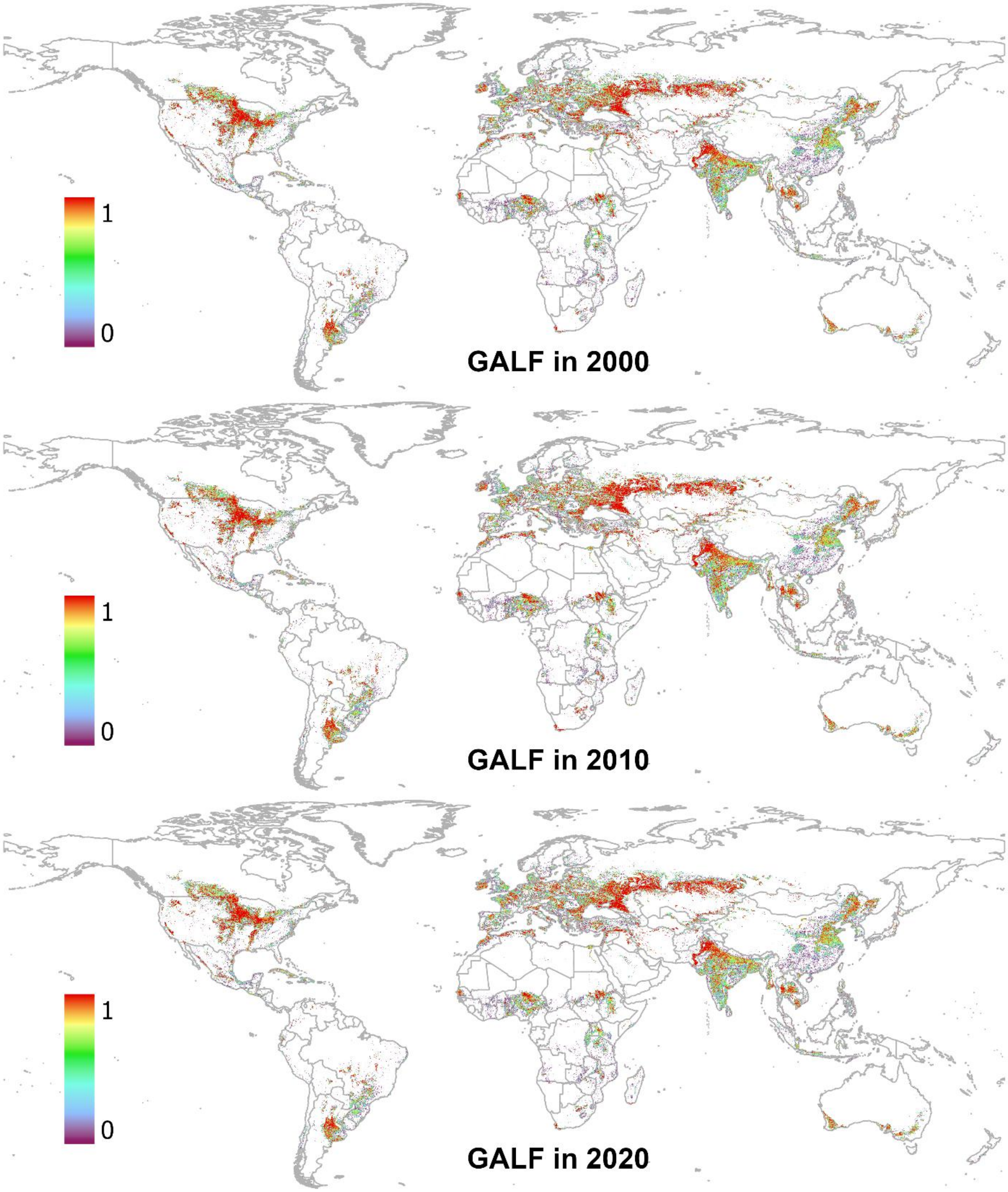

Fig. S7. 1-km Global Arable Land Fraction (GALF) maps for the years 2000, 2010, and 2020.

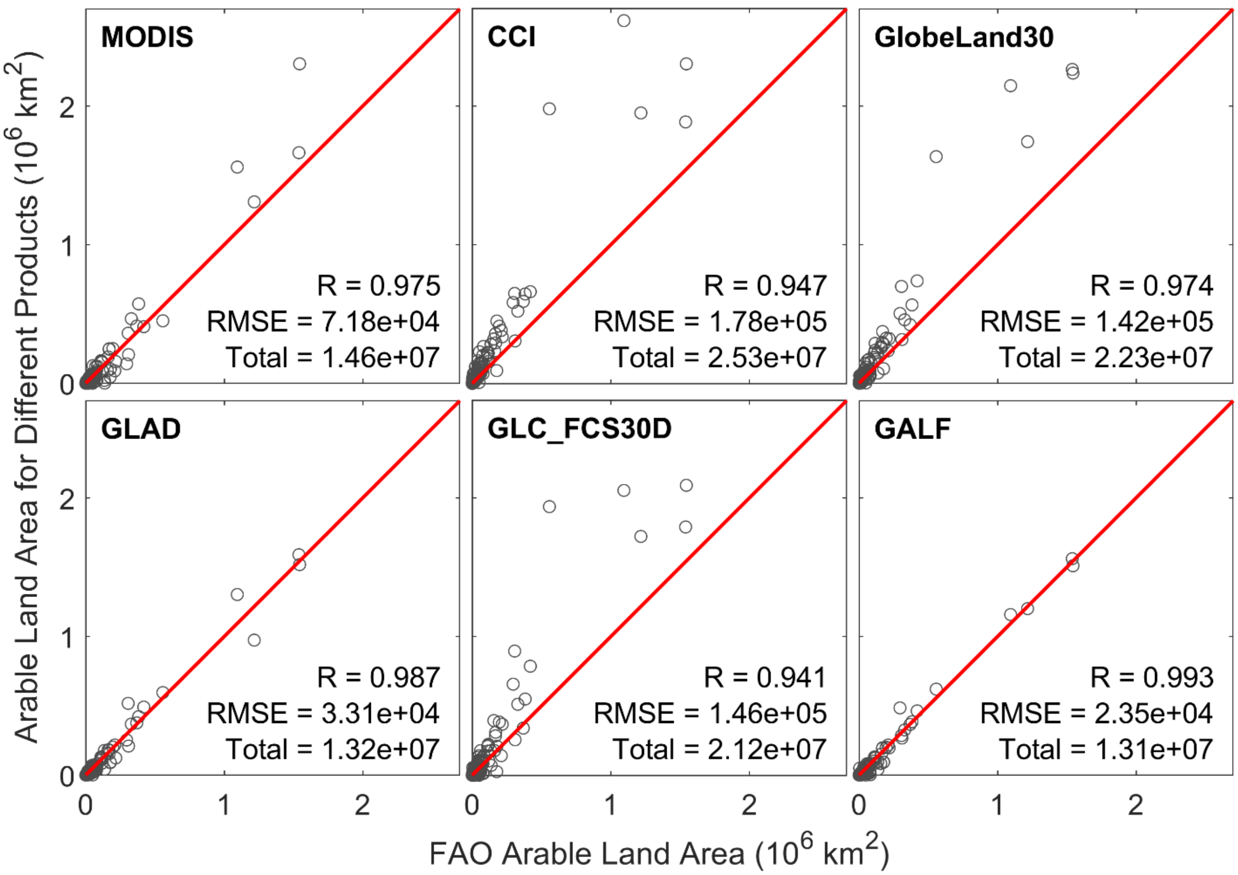

Fig. S8. Comparison of country-level arable land area (km^2) estimates from GALF and other products with FAO-reported arable land statistics in 2020, with countries lacking FAO reports excluded from the analysis. The total global arable land area reported by FAO is 1.38×10^7 km^2 in 2020.

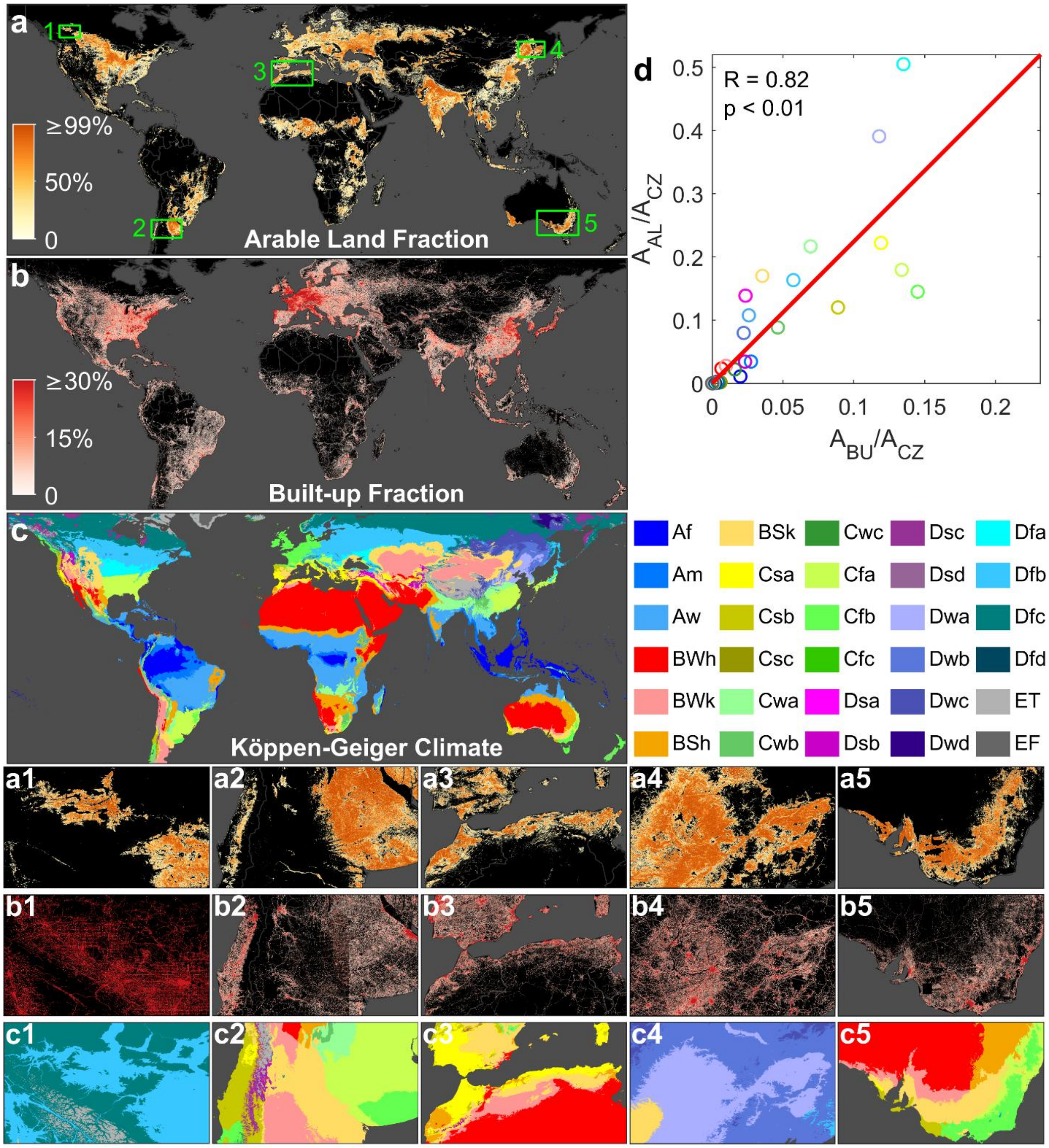

Fig. S9. Same as **Fig. 1** in the main text but using GLAD cropland and built data.

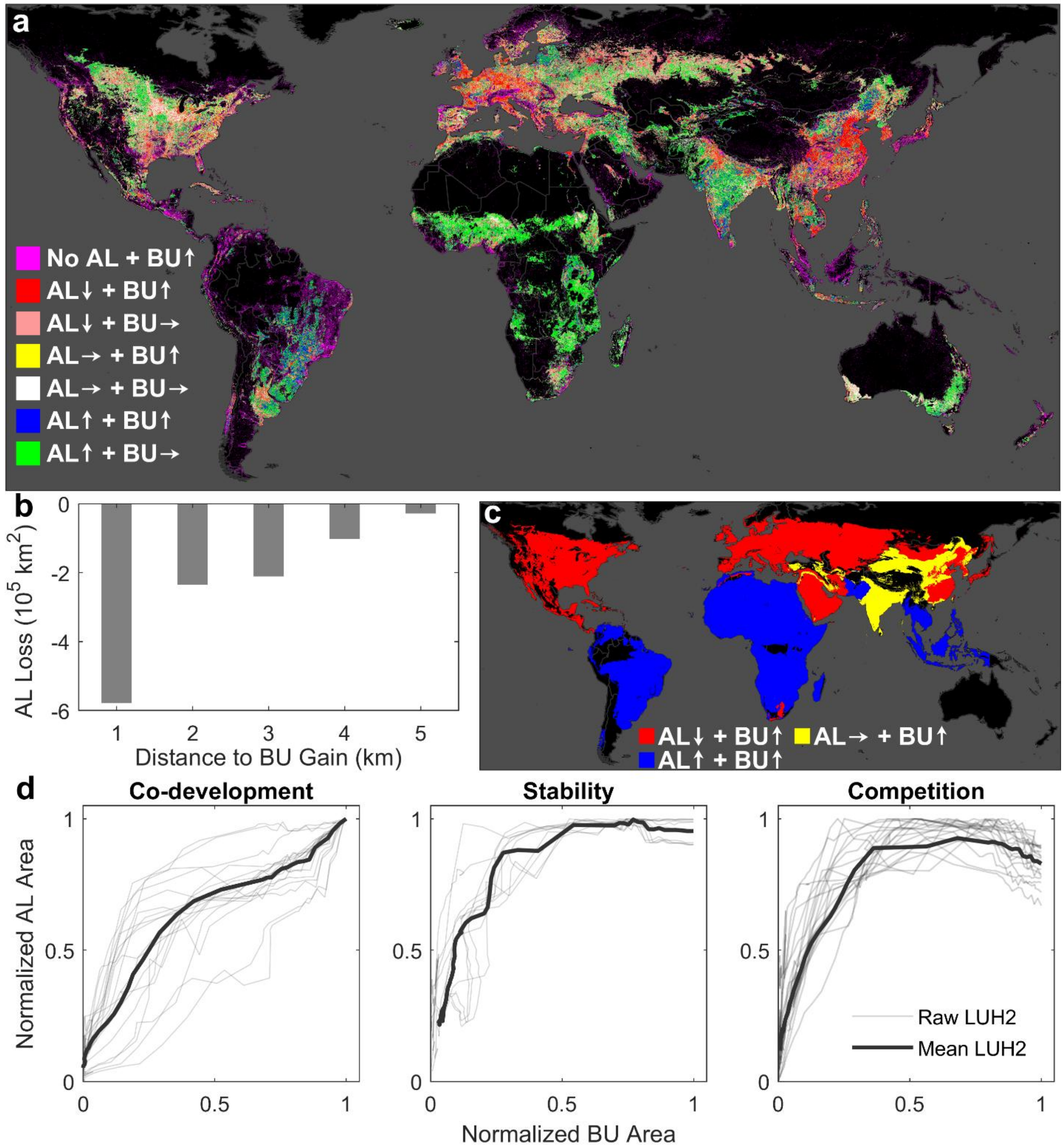

Fig. S10. Same as **Fig. 2** in the main text but using GLAD cropland and built data as well as LUH2 data.

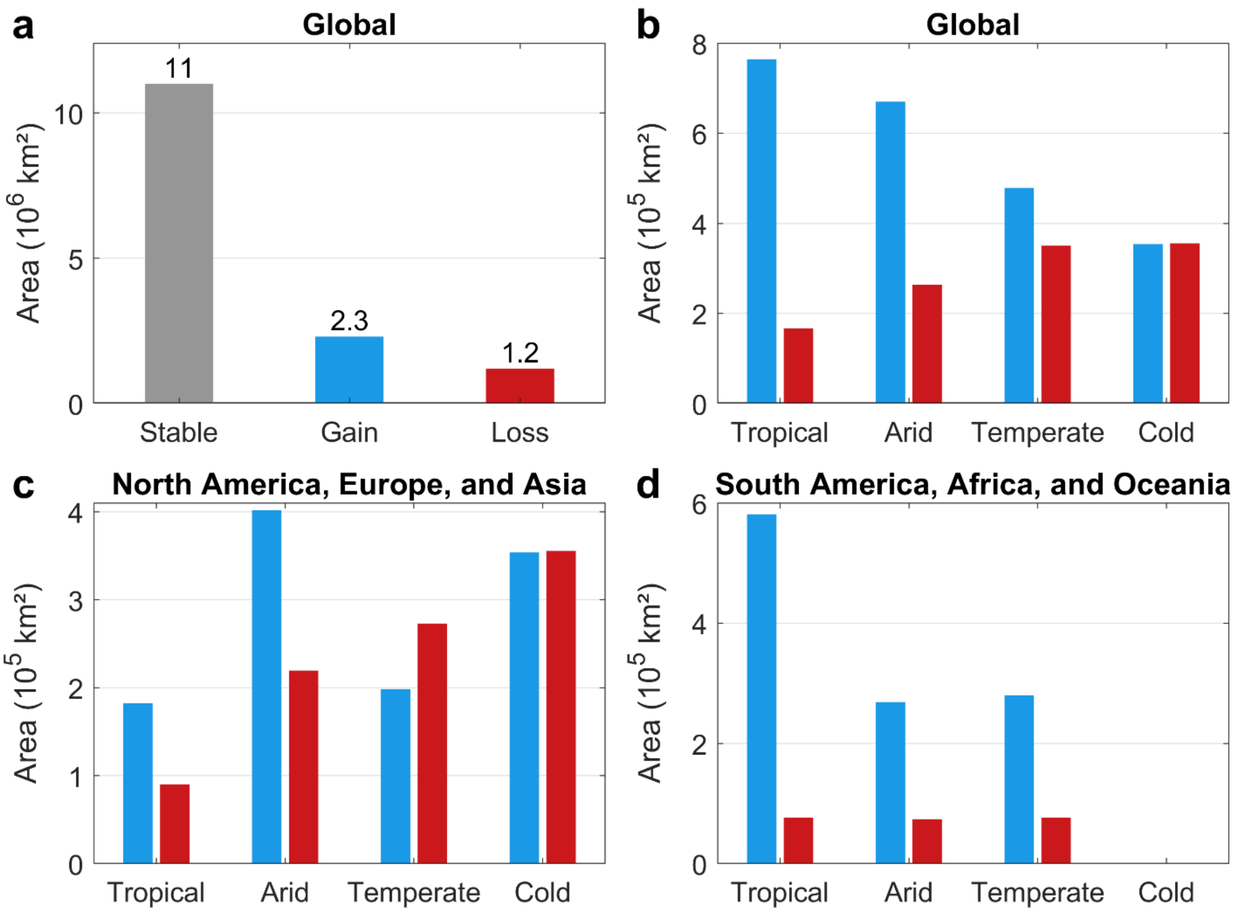

Fig. S11. Same as **Fig. 3** in the main text but using GLAD cropland data.

Supplementary Tables

Table S1. Specifications of five land cover products (MODIS, CCI, GlobeLand30, GLAD, and GLC_FCS30D) and FAO dataset. The definition of arable land used in this study follows the FAO's definition of arable land, which is highlighted in bold.

Dataset	Cropland Definition	Spatial Res.	Temporal Coverage
MODIS	Cropland (lands covered with temporary crops with harvest cycle less than one year. Includes areas of land temporarily fallow or left idle) and mosaic classes that mix cropland with other land cover types.	500 m	2001-2023
CCI	Rainfed cropland, herbaceous cover cropland, tree or shrub cover cropland, irrigated cropland, and mosaic classes that mix cropland with other land cover types.	300 m	1992-2020
GlobeLand30	Category includes paddy fields, irrigated dry land, rain-fed dry land, vegetable land, pasture planting land, greenhouse land, land and mainly for planting crops with fruit trees and other economic trees, as well as tea gardens, coffee gardens and other shrubs.	30 m	2000, 2010, 2020
GLAD	Land used for annual and perennial herbaceous crops for human consumption, forage (including hay) and biofuel. Perennial woody crops, permanent pastures and shifting cultivation are excluded from the definition. The fallow length is limited to 4 years for the cropland class.	30 m	2000, 2005, 2010, 2015, 2020
GLC_FCS30D	Rainfed cropland, irrigated cropland, herbaceous cover, and tree or shrub cover (orchard).	30 m	1985-2022
FAO	**Arable land includes areas under temporary agricultural crops (with multiple cropping counted once), temporary meadows for mowing or pasture, and land temporarily fallow.** Permanent crops refer to land cultivated with long-term crops that do not require annual replanting (e.g., cocoa, coffee, oil palm, and rubber), as well as land with flowering trees and shrubs (e.g., roses and jasmine) and nurseries, excluding those for forest trees that are classified as forest.	Country Level	1961-2023

Table S2. Scoring scheme for the five input land cover datasets. The agreement-score approach gives precedence to regions where multiple products consistently indicate arable land presence, whereas the binary-score approach prioritizes regions identified by the best products. The agreement and binary scores are identical for values of 0, 1, 2, 29, 30, and 31. Products are ordered by descending accuracy: A, B, C, D, and E. A value of 1 indicates arable land presence and 0 indicates absence.

Agreement Score	Binary Score	A	B	C	D	E
31	31	1	1	1	1	1
30	30	1	1	1	1	0
29	29	1	1	1	0	1

28	27	1	1	0	1	1
27	23	1	0	1	1	1
26	15	0	1	1	1	1
25	28	1	1	1	0	0
24	26	1	1	0	1	0
23	22	1	0	1	1	0
22	14	0	1	1	1	0
21	25	1	1	0	0	1
20	21	1	0	1	0	1
19	13	0	1	1	0	1
18	19	1	0	0	1	1
17	11	0	1	0	1	1
16	7	0	0	1	1	1
15	24	1	1	0	0	0
14	20	1	0	1	0	0
13	18	1	0	0	1	0
12	17	1	0	0	0	1
11	12	0	1	1	0	0
10	10	0	1	0	1	0
9	9	0	1	0	0	1
8	5	0	0	1	1	0
7	6	0	0	1	0	1
6	3	0	0	0	1	1
5	16	1	0	0	0	0
4	18	0	1	0	0	0
3	4	0	0	1	0	0
2	2	0	0	0	1	0
1	1	0	0	0	0	1
0	0	0	0	0	0	0

Table S3. Overall accuracy of the five input land cover products and GALF at continental and global scales, evaluated against 2010 reference samples. To avoid overinterpretation of marginal differences in ranking input products, only two decimal places were considered. As GALF is not independent of the reference samples, its accuracy is presented to assess the performance of the proposed method rather than for strict validation. The top three products are highlighted in red, green, and blue.

Continents	MODIS	CCI	GlobeLand30	GLAD	GLC_FCS30D	GALF
North America	0.871	0.786	0.767	0.816	0.706	0.874
Europe & North Asia	0.866	0.835	0.846	0.870	0.807	0.877
Oceania	0.936	0.867	0.917	0.933	0.839	0.943

Africa	0.876	0.759	0.862	0.872	0.851	0.899
East Asia	0.819	0.735	0.800	0.828	0.755	0.844
Southeast Asia	0.824	0.609	0.780	0.817	0.697	0.833
Southwest Asia	0.876	0.817	0.852	0.868	0.772	0.882
South Asia	0.766	0.703	0.754	0.800	0.705	0.808
South America	0.847	0.736	0.825	0.849	0.759	0.852
Global	0.869	0.784	0.808	0.842	0.755	0.877

Table S4. Overall accuracy of GALF and the five input land cover products at continental and global scales, evaluated against independent reference samples from 2020. The top three products are highlighted in red, green, and blue.

Continents	MODIS	CCI	GlobeLand30	GLAD	GLC_FCS30D	GALF
North America	0.921	0.848	0.850	0.885	0.782	0.919
Europe & North Asia	0.885	0.809	0.854	0.896	0.775	0.893
Oceania	0.917	0.857	0.931	0.919	0.783	0.922
Africa	0.882	0.692	0.824	0.825	0.800	0.864
East Asia	0.823	0.656	0.726	0.811	0.702	0.834
Southeast Asia	0.866	0.583	0.824	0.846	0.652	0.867
Southwest Asia	0.843	0.715	0.824	0.837	0.632	0.843
South Asia	0.838	0.731	0.820	0.836	0.760	0.843
South America	0.902	0.745	0.858	0.898	0.764	0.899
Global	0.887	0.765	0.839	0.871	0.763	0.887

Table S5. Same as **Table S4** but stratified by Köppen–Geiger climate zones. Climate zones with fewer than 100 reference samples were excluded from the analysis. The top three products are highlighted in red, green, and blue.

Climates	MODIS	CCI	GlobeLand30	GLAD	GLC_FCS30D	GALF
Af	0.947	0.697	0.909	0.942	0.792	0.941
Am	0.902	0.663	0.886	0.888	0.786	0.893
Aw	0.850	0.668	0.795	0.815	0.732	0.838

BWh	0.955	0.923	0.945	0.950	0.895	0.951
BWk	0.966	0.934	0.961	0.956	0.888	0.962
BSh	0.863	0.698	0.824	0.833	0.721	0.857
BSk	0.831	0.749	0.857	0.861	0.706	0.867
Csa	0.756	0.581	0.668	0.744	0.555	0.748
Csb	0.868	0.705	0.786	0.814	0.610	0.870
Cwa	0.838	0.679	0.734	0.794	0.701	0.823
Cwb	0.843	0.623	0.672	0.766	0.678	0.806
Cfa	0.804	0.625	0.631	0.753	0.598	0.804
Cfb	0.781	0.705	0.774	0.807	0.663	0.805
Cfc	0.991	0.912	0.982	0.982	0.876	0.991
Dsa	0.778	0.481	0.759	0.759	0.418	0.766
Dsb	0.916	0.619	0.914	0.896	0.546	0.934
Dsc	0.999	0.946	1	0.997	0.952	0.999
Dwa	0.782	0.701	0.736	0.783	0.710	0.807
Dwb	0.872	0.723	0.825	0.850	0.745	0.877
Dwc	0.994	0.870	0.992	0.993	0.910	0.995
Dwd	1	0.983	1	1	1	1
Dfa	0.785	0.711	0.711	0.724	0.668	0.788
Dfb	0.855	0.762	0.772	0.837	0.682	0.860
Dfc	0.996	0.970	0.991	0.996	0.950	0.997
ET	0.998	0.926	0.997	0.998	0.954	0.998
EF	1	0.999	1	1	1	1
Average	0.891	0.764	0.851	0.875	0.759	0.891

Reference

46. Gong, P. *et al*. Finer resolution observation and monitoring of global land cover: First mapping results with Landsat TM and ETM+ data. *Int. J. Remote Sens.* **34**, 2607–2654 (2013).
47. Friedl, M. A. *et al*. Global land cover mapping from MODIS: algorithms and early results. *Remote Sens. Environ.* **83**, 287–302 (2002).
48. European Space Agency. Climate Change Initiative Land Cover. http://maps.elie.ucl.ac.be/CCI/viewer/index.php (2015).
49. Chen, J. *et al*. Global land cover mapping at 30 m resolution: A POK-based operational approach. *ISPRS J. Photogramm. Remote Sens.* **103**, 7–27 (2015).
50. Potapov, P. *et al*. The global 2000–2020 land cover and land use change dataset derived from the Landsat archive: first results. *Front. Remote Sens.* **3**, 856903 (2022).
51. Zhang, X. *et al*. GLC_FCS30D: The first global 30-m land-cover dynamic monitoring product with a fine classification system from 1985 to 2022 using dense time-series Landsat imagery and continuous change-detection method. *Earth Syst. Sci. Data Discuss.* **2023**, 1–32 (2023).
52. Kerr, J. & Cihlar, J. Land use and cover with intensity of agriculture for Canada from satellite and census data. *Glob. Ecol. Biogeogr.* **12**, 161–172 (2003).
53. Jung, M. *et al*. Exploiting synergies of global land cover products for carbon cycle modeling. *Remote Sens. Environ.* **101**, 534–553 (2006).
54. Ramankutty, N. *et al*. Farming the planet: 1. Geographic distribution of global agricultural lands in the year 2000. *Glob. Biogeochem. Cycles* **22**, GB1003 (2008).
55. Fritz, S. *et al.* Cropland for sub-Saharan Africa: A synergistic approach using five land cover data sets. *Geophys. Res. Lett.* **38**, L04402 (2011).
56. Fritz, S. *et al.* Mapping global cropland and field size. *Glob. Change Biol.* **21**, 1980–1992 (2015).
57. Lu, M. *et al.* A cultivated planet in 2010: 1. The global synergy cropland map. *Earth Syst. Sci. Data* **12**, 1913–1928 (2020).
58. Tubiello, F. *et al*. A new cropland area database by country circa 2020. *Earth Syst. Sci. Data* **15**, 4997–5015 (2023).
59. Zhao, Y. *et al*. Towards a common validation sample set for global land-cover mapping. *Int. J. Remote Sens.* **35**, 4795–4814 (2014).
60. Fritz, S. *et al.* A global dataset of crowdsourced land cover and land use reference data. *Sci. Data* **4**, 170075 (2017).
61. Stehman, S. *et al*. Validation of the US Geological Survey's Land Change Monitoring, Assessment and Projection (LCMAP) Collection 1.0 annual land cover products, 1985–2017. *Remote Sens. Environ.* **265**, 112646 (2021).
62. Zhao, T. *et al.* Assessing the accuracy and consistency of six fine-resolution global land cover products using a novel stratified random sampling validation dataset. *Remote Sens.* **15**, 2285 (2023).

63. FAO. FAOSTAT land use [Dataset]. http://www.fao.org/faostat/en/#data/RL (2019).
64. U.S. Department of State, Office of the Geographer. Large Scale International Boundaries (LSIB) – Simplified (2017). Available at: https://developers.google.com/earth-engine/datasets/catalog/USDOS_LSIB_SIMPLE_2017
65. World Bank. Global strategy to improve agricultural and rural statistics. *Econ. Sect. Work* **56719-GLB** (2011).
66. Tong, X. *et al.* Global area boom for greenhouse cultivation revealed by satellite mapping. *Nat. Food* **5**, 513–523 (2024).
67. Gómez-Galán, M. *et al.* Assessment of postural load during melon cultivation in Mediterranean greenhouses. *Sustainability* **10**, 2729 (2018).
68. Mendoza-Fernández, A. *et al.* The role of technology in greenhouse agriculture: Towards a sustainable intensification in Campo de Dalías (Almería, Spain). *Agronomy* **11**, 101 (2021).
69. Woodcock, C. E. *et al*. Free access to Landsat imagery. *Science* **320**, 1011 (2008).
70. Huete, A. et al. Overview of the radiometric and biophysical performance of the MODIS vegetation indices. *Remote Sens. Environ.* **83**, 195–213 (2002).
71. Anderson, J. R. *A Land Use and Land Cover Classification System for Use with Remote Sensor Data* Vol. 964 (US Government Printing Office, 1976).
72. Di Gregorio, A. *Land Cover Classification System: Classification Concepts and User Manual: LCCS* (Food & Agriculture Org., 2005).
73. European Commission. Joint Research Centre. *GHSL Data Package 2023*. Publications Office of the European Union, https://data.europa.eu/doi/10.2760098587 (2023).
74. Pesaresi, M. *et al.* Advances on the Global Human Settlement Layer by joint assessment of Earth Observation and population survey data. *Int. J. Digit. Earth* **17**, 2390454 (2024).
75. Garnelo, M. & Shanahan, M. Reconciling deep learning with symbolic artificial intelligence: representing objects and relations. *Curr. Opin. Behav. Sci.* **29**, 17–23 (2019).
76. Phiri, D. *et al.* Sentinel-2 data for land cover/use mapping: A review. *Remote Sens.* **12**, 2291 (2020).
77. Everingham, M. *et al***.** The Pascal Visual Object Classes (VOC) Challenge. *Int. J. Comput. Vis.* **88**, 303–338 (2010).
78. Ronneberger, O. *et al*. U-net: Convolutional networks for biomedical image segmentation. *Lect. Notes Comput. Sci.* **9351**, 234–241 (2015).
79. Beck, H. E. *et al.* High-resolution (1 km) Köppen–Geiger maps for 1901–2099 based on constrained CMIP6 projections. *Sci. Data* **10**, 724 (2023).
80. Beck, H. E. *et al.* Present and future Köppen-Geiger climate classification maps at 1-km resolution. *Sci. Data* **5**, 180214 (2018).
81. Kottek, M., *et al.* World map of the Köppen-Geiger climate classification updated. *Meteorol. Z.* **15**, 259–263 (2006).
82. Peel, M. C., *et al*. Updated world map of the Köppen-Geiger climate classification. *Hydrol. Earth Syst. Sci.* **11**, 1633–1644 (2007).
83. Mahlstein, I., *et al.* Pace of shifts in climate regions increases with global temperature. *Nat. Clim. Change* **3**, 739–743 (2013).

84. Klein G. *et al*. Anthropogenic land use estimates for the Holocene – HYDE 3.2. *Earth Syst. Sci. Data* **9**, 927–953 (2017).
85. Hurtt, G. C. *et al*. Harmonization of global land-use change and management for the period 850–2100 (LUH2) for CMIP6. *Geosci. Model Dev.* **13**, 5425–5464 (2020).